nature materials

ARTICLES

PUBLISHED ONLINE: 19 JUNE 2017 | DOI: 10.1038/NMAT4920

Emergence of an enslaved phononic bandgap in a non-equilibrium pseudo-crystal

Nicolas Bachelard[1†], Chad Ropp[1†], Marc Dubois[1], Rongkuo Zhao[1], Yuan Wang[1,2] and Xiang Zhang[1,2,3*]

Material systems that reside far from thermodynamic equilibrium have the potential to exhibit dynamic properties and behaviours resembling those of living organisms. Here we realize a non-equilibrium material characterized by a bandgap whose edge is enslaved to the wavelength of an external coherent drive. The structure dynamically self-assembles into an unconventional pseudo-crystal geometry that equally distributes momentum across elements. The emergent bandgap is bestowed with lifelike properties, such as the ability to self-heal to perturbations and adapt to sudden changes in the drive. We derive an exact analytical solution for both the spatial organization and the bandgap features, revealing the mechanism for enslavement. This work presents a framework for conceiving lifelike non-equilibrium materials and emphasizes the potential for the dynamic imprinting of material properties through external degrees of freedom.

Materials in nature spontaneously form through microscopic and collective interactions. This self-organization process is often a source of wonder and a catalyst for scientific inspiration. By understanding crystal growth, people have been able to artificially synthesize materials with high purity[1], and subsequently invent new composite[2,3] and crystalline forms[4–6]. Crystals are examples of the rigid structures that form by static self-assembly, the process through which order arises in an equilibrium state[7]. Still, nature shows us that order can arise far from thermodynamic equilibrium, as seen in living cells[8], the swarming and flocking of animals[9–12], and even weather patterns[13]. These systems arise and are sustained outside of thermodynamic equilibrium through the collective dissipation of energy (that is, irreversible loss)[14] in a process known as dynamic self-assembly. Remarkably, this self-sustaining process produces structures exhibiting lifelike behaviours[15], such as the ability to self-heal[16], self-adapt to changes in the environment[17–19], and self-replicate[20]—with features that might evolve linked to dissipative history[21,22]. Non-equilibrium materials, therefore, provide a foundation for creating artificial systems that are inspired by nature and mimic living organisms[23–29].

Materials research is ultimately devoted to the study of physical properties. For materials that reside in thermodynamic equilibrium, macroscopic properties often result from the microscopic organization (for example, photonic bandgaps in opals[30,31]) or the properties of the microscopic elements (for example, resonance-based phononic bandgaps[32,33]). The question arises whether these properties can be imprinted directly into a material without requiring the systematic engineering of the material's microscopic features. Towards this end, non-equilibrium materials can provide a solution. Non-equilibrium systems are inherently open to their environment and the necessary input of energy offers a route for the external modification of material responses. This open channel has been utilized to tune the geometry of non-equilibrium structures, for example by changing the flow rate[34] or frequency[17–19,28,35] of the drive. However, beyond the tuning of geometry, exploiting this channel to dynamically imprint physical properties into non-equilibrium materials has never been investigated. Such ability could enable external degrees of freedom to direct self-organization and simultaneously encode macroscopic properties.

In this article, we report the first demonstration of a non-equilibrium material with an emergent Bragg-type bandgap that is enslaved to the wavelength of an external coherent source. The system consists of an array of scattering particles sitting in a viscous liquid and confined within a one-dimensional single-mode waveguide. These particles dynamically self-assemble towards a configuration that equally distributes momentum along the structure. The resulting order corresponds to an unconventional pseudo-crystal exhibiting a phononic bandgap, whose band edge is enslaved to the wavelength of the acoustic source. The structure resides far from equilibrium, reaching a steady state that moves forward in time and constantly dissipates the particles' kinetic energy. Remarkably, the lifelike behaviours often observed in non-equilibrium structures are here bestowed to the emergent bandgap itself. This is manifested in its ability to self-heal to mechanical perturbations and self-adapt to changes in the drive wavelength. Seldom achieved for non-equilibrium systems[36], we are able to derive an exact analytical solution for the non-equilibrium steady state. This solution is confirmed experimentally and emphasizes the central role of wave coherence in bandgap enslavement. In addition, our design offers the ability to investigate the transient process of dynamic self-assembly, from which we experimentally confirm dynamic attraction and subsequent phase-space collapse. Finally, we stress that our analytic solution is completely general and applicable to any classical wave system.

Emergence of an enslaved bandgap

Our experiment consists of a single-mode acoustic waveguide filled with 12 mobile particles that sit in the meniscus of a viscous liquid (see Methods). These particles are put in motion by the continuous acoustic pressure exerted by a coherent and unidirectional drive field (Fig. 1a). The system dynamically self-assembles into a non-equilibrium structure, which coincides with the emergence of a phononic bandgap with its higher-wavelength band edge enslaved to λ_0, the wavelength of the source

[1]NSF Nanoscale Science and Engineering Center, 3112 Etcheverry Hall, University of California, Berkeley, California 94720, USA. [2]Materials Sciences Division, Lawrence Berkeley National Laboratory, 1 Cyclotron Road, Berkeley, California 94720, USA. [3]Department of Physics, King Abdulaziz University, Jeddah 21589, Saudi Arabia. †These authors contributed equally to this work. *e-mail: xzhang@me.berkeley.edu

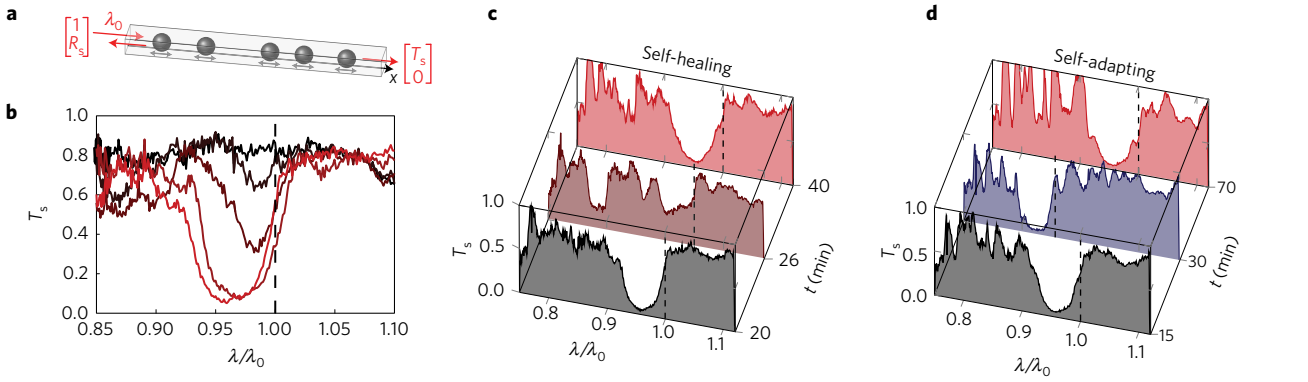

Figure 1 | Bandgap emergence in a non-equilibrium material. a, Schematic showing a single-mode waveguide filled with mobile scattering particles in a viscous liquid. The particles move along the *x*-direction in response to a coherent field, wavelength λ_0, incident from the left. The red column vectors indicate the forward and backward propagating field intensities across the structure, where R_S is the reflection coefficient and T_S is the transmission coefficient. **b**, Time evolution of a transmission spectrum showing bandgap emergence. Curves correspond to spectra taken at $t = 0, 5, 10, 20$ and 30 min (black to red). **c**, Bandgap self-healing to a mechanical perturbation, perturbed at $t = 25$ min. Spectra are taken before (black), immediately after (dark red), and following self-healing (red). **d**, Bandgap self-adapting to changes in the external drive wavelength. Spectra are taken when the drive wavelength is λ_0 (black), $0.9\lambda_0$ (dark blue), and returned to λ_0 (red). The drive is initially switched to $0.9\lambda_0$ at $t = 18$ min, then switched back to λ_0 at $t = 42$ min.

(Fig. 1b and Supplementary Movie 1). This bandgap is Bragg-like and arises through the collective interferences between the sub-wavelength scatterers. At $t = 0$ the source is turned on and the particles begin to move in various directions. Eventually, they self-organize into a mechanical steady state—the separations between particles become fixed, while the assembly collectively moves forward in time. Since the kinetic energy of this collective motion is continuously dissipated through viscous friction, our steady state never reaches thermodynamic equilibrium. In addition to ensuring non-equilibrium operation, the viscosity stabilizes the steady state by enforcing overdamped particle motion (see Methods). Remarkably, the enslaved bandgap emerges regardless of the initial placement of the particles, even when the steady state is organized differently (Supplementary Fig. 1).

The emerging bandgap exhibits several lifelike behaviours—it self-heals to mechanical perturbations (Fig. 1c and Supplementary Movie 2) and re-emerges at different wavelengths in response to sudden changes in the drive (Fig. 1d and Supplementary Movie 3). Although geometric structures arising through dynamic self-assembly often exhibit self-healing and self-adaptive characteristics[15], here these lifelike properties are readily bestowed to the bandgap feature itself.

Pseudo-crystal formation

The mechanisms that govern the dynamic self-assembly in our system are revealed by monitoring the trajectories of individual particles (see Methods for experimental details). During self-assembly, the velocities of the individual particles evolve such that the total kinetic energy of the ensemble increases during the initial assembly and relaxes as the system approaches its steady-state organization (Supplementary Fig. 2). In contrast to conventional Bragg-type bandgap materials emerging from crystalline order[37], our structure appears pseudo-crystalline as a consequence of the coherent and equal distribution of momentum amongst the particles (Fig. 2). To better visualize this pseudo-crystalline order, we track the particles' positions during the self-assembly process and decompose their centre-to-centre distance as $x_n - x_{n-1} = D_S + p_n\lambda_0/2 + d_n$, where D_S is the width of each particle, p_n is a distribution of positive integers, and d_n is the residual separation between particles, modulo $\lambda_0/2$. In this definition, $n \in [1, N]$ for x_n, while $n \in [2, N]$ for p_n and d_n, where N is the number of particles.

The system evolves towards a non-equilibrium steady state with a non-uniform p_n distribution, which describes the pseudo-crystal geometry (Fig. 2a). This geometry fulfils the phase requirement imposed by the coherent field, producing the bandgap response. Self-organization is mediated by the feedback between particle motion and wave scattering. The coherent field exerts acoustic pressure on the particles, whose motion in turn modifies the scattered field. Particle interactions are thus mediated by the field, whose intensity interferences are unchanged by additional $p_n\lambda_0/2$ separations. The preservation of λ_0-coherence is confirmed experimentally by the π-phase degeneracy observed in our structure. Depending on the initial configuration, any distribution of p_n can be reached (Supplementary Fig. 1), indicating that our system can self-assemble into many equivalent pseudo-crystalline geometries with similar bandgap responses. While dynamic self-assembly commonly arises through hydrodynamic interactions[17,19,25,27,28,34], here the assembly is entirely mediated by the coherent field, which produces multiple interaction length scales depending on p_n. Since particles are only weakly absorbing (see Methods), and our system is confined into a single waveguide mode, the coherence is preserved along the structure. By preserving mode coherence, our system is in contrast to other wave-based approaches for self-assembly, such as optical binding[38]. These approaches utilize scattering into multiple spatial modes to produce long-distance coupling between particles[39,40], but as a result lose the spatial coherence required for bandgap emergence.

The time evolution of our system is characterized by the attraction towards a configuration with a nearly constant, but monotonically decreasing residual spacing, d_n (Fig. 2b and inset). This organization is in further contrast to conventional bandgap crystals that, being periodic, would have a constant d_n. The asymmetry observed in d_n originates from the open boundary conditions and the unidirectional transfer of momentum from the source to the ensemble, which produces the overall one-way motion. This asymmetry is also observed in the evolution of d_n, as displayed by the slower temporal response and pronounced oscillations for larger n (Supplementary Fig. 3). Snapshots of d_n at different times also reveal the connection between particle order and bandgap self-healing and self-adaptability. Self-healing of the bandgap coincides with self-healing of d_n (Fig. 2c and Supplementary Fig. 4), while bandgap emergence at different wavelengths is reflected by an overall shift in d_n (Fig. 2d and Supplementary Fig. 5).

Theoretical description of the emergent bandgap

At steady state the system self-organizes into a pseudo-crystalline geometry that equally distributes momentum across all particles. In our theoretical model, we consider lossless scatterers and a

one-dimensional geometry, which maintains the spatiotemporal coherence of the drive field throughout multiple scattering events. Losses can be taken into account numerically (see Methods), showing similar pseudo-crystal self-assembly (Supplementary Fig. 6). Wave coherence enforces a steady-state condition in which each particle experiences the same pressure force, $F_S = 2R/(1+(N-1)R)$ (see Methods), where R is the reflection coefficient in intensity for an individual particle. Since the velocity of the particles at steady state is proportional to F_S, the ensemble speed decreases with the number of particles. Uniform momentum transfer is achieved when the average field intensity, $\langle I_n \rangle$, between particle $n-1$ and n, decays according to the arithmetic progression (Fig. 3a,b):

$$\langle I_n \rangle = 1 + F_S\left(\frac{N}{2} + (1-n)\right), \quad \forall n \in [2,N] \tag{1}$$

where the difference in average intensity across each particle, F_S, defines the pressure force. The intensity distribution of equation (1) requires a collective phase organization described by:

$$\Psi_n + \Phi_s = \pi - \frac{1}{2}\operatorname{asin}\left(\sqrt{\frac{1+(N-n)R}{1+(N-n)}}\right)$$

$$-\frac{1}{2}\operatorname{asin}\left(R\sqrt{\frac{1+(N-n)}{1+(N-n)R}}\right) \tag{2}$$

where $\Psi_n = 2\pi d_n/\lambda_0$, Φ_s is the phase accumulated from crossing a particle, and the residual phase, $\Psi_n + \Phi_s$, is defined modulo π (inset of Fig. 3a). The full derivations of equations (1) and (2) are provided in the Supplementary Information. Equation (2) describes a monotonically decreasing trend (Fig. 3c), which agrees well with the experimental data when $R = 0.04$ (see Methods). Remarkably, the phase distribution in equation (2) depends only on R and the difference $N-n$, confirming that the residual phase between particles is locked and the d_n are strictly bound to λ_0. In addition, by allowing a π-ambiguity in the total phase $\Phi_n + \Phi_s = \Psi_n + \Phi_s + p_n\pi$ (inset of Fig. 3a), equation (2) also confirms the pseudo-crystal organization observed in Fig. 2. Importantly, equation (2) is well defined for $0 < R < 1$ and $n \leq N$, which stresses the existence of solutions for all experimental conditions.

The phase-locked organization described by equation (2) produces an unconventional bandgap material, whose higher-wavelength edge is enslaved to λ_0 and whose lower edge expands to lower wavelengths with an increasing R (Fig. 3d). This bandgap feature matches remarkably well with the experimentally observed bandgap for $R = 0.04$. Bandgap enslavement at λ_0 can be understood by considering long systems ($N \to \infty$) and particles close to the source, which simplifies the residual phase: $\Psi_n + \Phi_s \to \pi - \operatorname{asin}(\sqrt{R})$. We assume that the non-uniform p_n can be described by a random variable with a median $\bar{p}$ and a standard deviation σ_p (Fig. 3e and inset), such that the total phase reads $\Phi_n + \Phi_s \to (\bar{p}+1)\pi - \operatorname{asin}(\sqrt{R})$. Using an effective Bloch crystal description, we obtain the location of the band edges (see Supplementary Information):

$$\begin{cases} \lambda_+ = \lambda_0 \\ \lambda_- = \lambda_0 \dfrac{(\bar{p}+1)\pi - \operatorname{asin}(\sqrt{R})}{(\bar{p}+1)\pi + \operatorname{asin}(\sqrt{R})} \end{cases} \tag{3}$$

where the higher-wavelength edge, λ_+, is enslaved to the drive wavelength independent of all other system parameters. Equation (3) is valid for large dispersions in p_n (Fig. 3f). Despite increasing randomness in p_n, transmission curves with the same $\bar{p}$ emerge with similar bandgaps (Supplementary Fig. 1). The accuracy of equation (3) is confirmed by the full-width at half-maximum measured

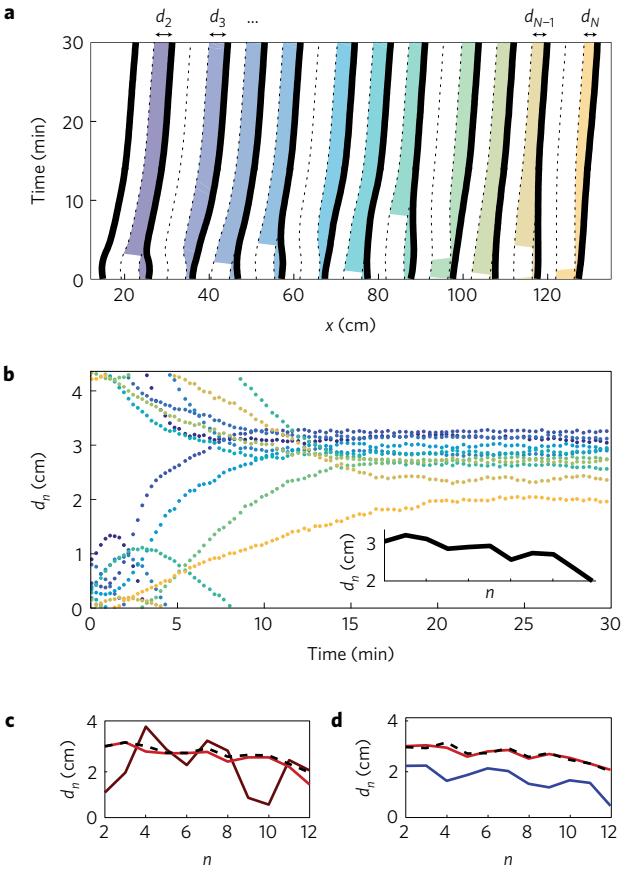

Figure 2 | Pseudo-crystal formation. a, Raw data showing the trajectory of the particle positions over time (black lines). The particles are initially regularly spaced by 12.5 cm along the waveguide and subsequently self-organize into a pseudo-crystal. The coloured regions label the d_n and the dashed lines separate the different $p_n\lambda_0/2$. **b**, Plot of d_n as a function of time. Colours correspond to the regions labelled in **a**. The inset plots d_n at steady state ($t = 30$ min). **c**, Plot of d_n for the self-healing data set of Fig. 1c with corresponding colours. These data show the d_n organization before (dashed black curve, $t = 20$ min), immediately after (dark red curve, $t = 26$ min), and self-healed from (red curve, $t = 30$ min) perturbation. **d**, Plot of d_n for the self-adaptation data set of Fig. 1d with corresponding colours. These data show the d_n organization with the source driven initially at λ_0 (dashed black curve, $t = 15$ min), after switching to $0.9\lambda_0$ (dark blue curve, $t = 30$ min), and after returning to λ_0 (red curve, $t = 70$ min).

from experiment ($0.07\lambda_0$), which is close to the value obtained from equation (3) ($\lambda_+ - \lambda_- = 0.06\lambda_0$) with $R = 0.04$ and $\bar{p} = 1$. Band-edge enslavement to the drive also ensures that functionally equivalent bandgaps emerge even after large perturbations that may change p_n, but keep $\bar{p}$ constant. Changes in $\bar{p}$, however, will result only in wider or narrower bandgaps, while λ_+ remains locked to λ_0. A qualitative understanding of band-edge enslavement can be obtained by considering the Bloch crystal description for infinite systems with uniform p_n. Here, the linear decrease in intensity along the length of the structure derived in equation (1) corresponds to an infinitely long exponential decay, which must occur at the higher-wavelength band-edge transition between propagating and evanescent waves (see Supplementary Information).

Phase-space attraction during dynamic self-assembly

We consider several benchmark cases consisting of $N = 3$ particles with varied initial conditions to investigate transient behaviour. The transient processes are revealed by the progression in the position (x) and momentum (p) phase-space[41], which in our system is

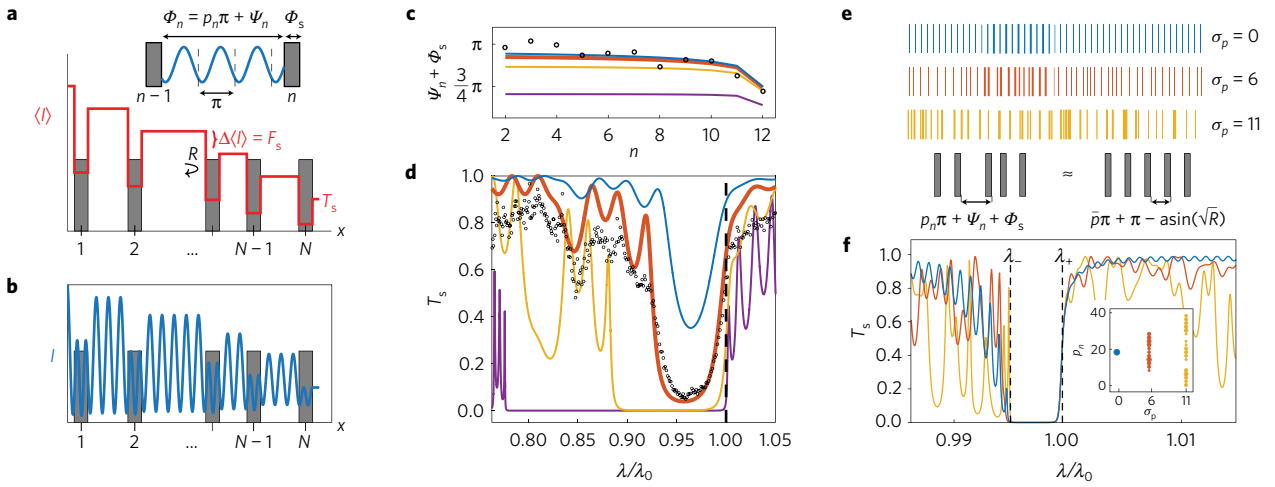

Figure 3 | Theoretical prediction of bandgap emergence out of equilibrium. a, The steady-state profile of the averaged field intensity, $\langle I \rangle$, as a function of position along the waveguide, x. This profile results from the self-organization of particles (grey rectangles, with individual intensity reflection coefficient R) such that wave momentum is equally shared, and the intensity drop across each particle is equal to $\Delta\langle I \rangle = F_S$. Inset labels our naming conventions used throughout the paper. **b**, Example steady-state intensity profile, $I(x)$, for particles separated by a non-uniform distribution of integer half wavelengths, $p_n\lambda_0/2$. **c**, Phase accumulated at steady state between particles $n-1$ and n, modulo π, for different reflection coefficients, $R = 0.01$ (blue), 0.04 (red), 0.16 (yellow), 0.64 (purple). Black circles correspond to experimental data from the inset of Fig. 2b. **d**, Corresponding transmission spectra from **c**, with a p_n distribution equal to that of the experiment from Fig. 2a. Experimental data is overlaid as black circles (for R estimated to be 0.04). **e**, Illustration of three $N = 50$ structures with $R = 0.02$ and identical $\bar{p} = 20$, but increasing standard deviation, σ_p. These structures are modelled by equivalent Bloch crystals (see grey illustration). **f**, The transmission spectrum of each structure, with the same colour as in **e**, plotted with black dashed lines corresponding to the location of the band edges predicted analytically from equation (3). The inset is a histogram of the p_n distributions as a function of σ_p for the three structures shown in **e**. The size of each data point corresponds to the number of particle separations with the same p_n.

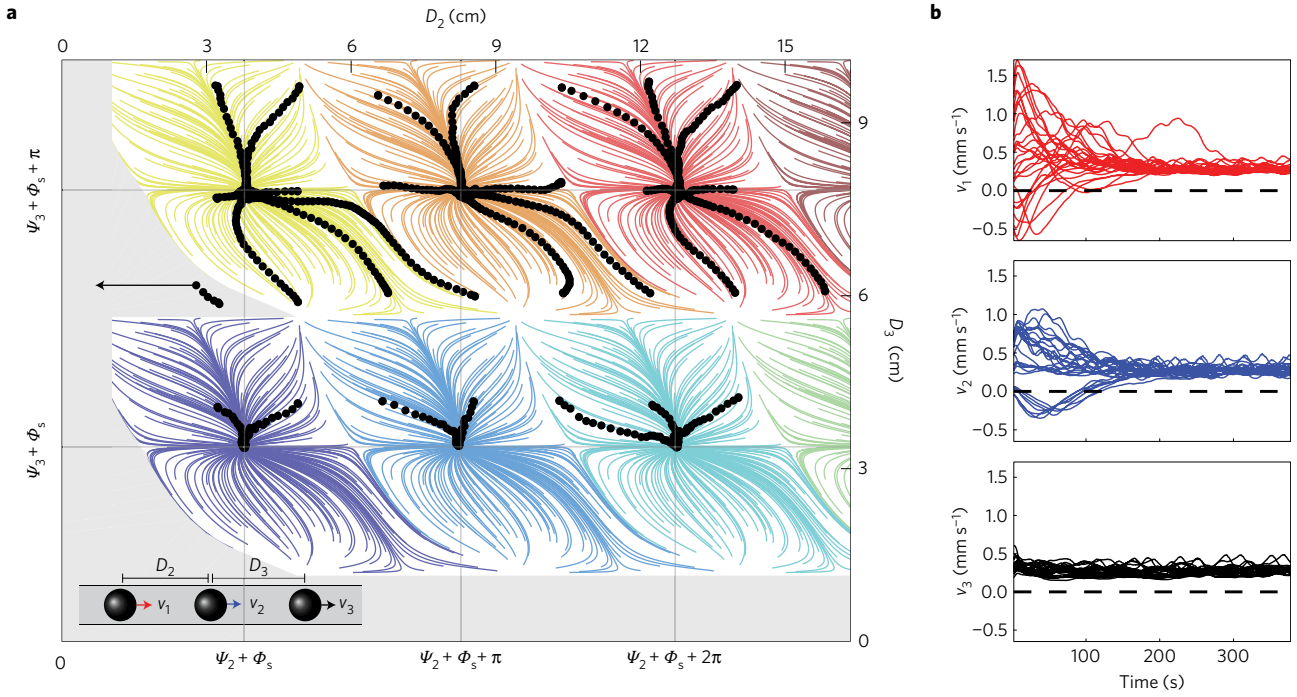

Figure 4 | Position and momentum phase-space collapse. a, Graph of the position phase-space for a $N = 3$ system. The secondary axes label the corresponding real-space, with D_2 and D_3 defined in the inset. The coloured lines are the trajectories of particle separations during self-organization, obtained numerically. Different colours denote the different basins of attraction that collapse to the same steady state described by equation (2). The black data points are trajectories obtained experimentally from 29 different initial configurations, showing similar phase-space collapse. The greyed area represents the region where attractors force particles to collide, which is confirmed experimentally (data set with black arrow). **b**, The velocity of each particle (obtained using a 20 s running average) measured experimentally as a function of time (colours and labels correspond with the inset of **a**). Each particle in all data sets (the colliding data set excluded) are shown converging to a common steady-state velocity.

equivalent to studying $[\Phi_i(t), v_j(t)]$ for i in $\{1, 2\}$ and j in $\{1, 3\}$. The particles' trajectories are attracted in position-space to steady states that are identical to equation (2) and in momentum-space to velocities that are uniform (Fig. 4). We find that experimental trajectories closely follow the numerical model (see Methods). The observation of these position and momentum-space attractors

emphasizes the collapse of the system phase-space, which is a signature of dynamic self-assembly[15].

These attractors support the continuous attraction towards steady state and ultimately bestow our system with the robust self-healing and self-adaptive properties observed in experiment. Each of these non-equilibrium steady states are fed by their own basins of attraction, which are asymmetric, but periodic in position-space as anticipated by the spatial degeneracies observed in Fig. 2. The basins of attraction fill the position phase-space, ensuring the emergence of functionally similar bandgap structures, regardless of the initial placement or any perturbation of the system. This robust behaviour is maintained as long as the separations between particles do not become so close that their attractors require them to cross one another (grey region in Fig. 4a). Although we probe the phase-space response using three particles, similar dynamics occur at higher dimensions.

Conclusion

In this work, we demonstrated an approach for realizing bandgap materials that reside far from equilibrium and emerge enslaved to an external drive. Our system self-organizes into an unconventional pseudo-crystal geometry through coherent-momentum sharing. In contrast to approaches using static self-assembly[42] or top-down fabrication[43] that typically result in rigid structures with fixed properties, dynamic self-assembly enables the creation of lifelike structures with dynamically imprinted properties. We observed the emergence of a phononic bandgap with the ability to self-heal and spontaneously self-adapt to changes in the source wavelength. Despite the existence of many spatial attractors, our system always self-organizes to form a transmission bandgap enslaved at its higher-wavelength edge to the wavelength of the drive. Since our system relies on wave interferences, our approach could be extended to other wave systems (for example, electromagnetic) to produce bandgap materials at different length scales.

Although dynamic self-assembly has been studied for decades, its underlying principles are only partially understood and, in particular, the role of entropy production in the emergence of order far from equilibrium is still debated[14,44–46]. Resolving such uncertainties is made particularly challenging due to the scarcity of physical systems that are both complex enough to self-organize outside of equilibrium and simple enough to be described analytically[36]. By solving the non-equilibrium steady-state order for an arbitrarily large number of individual elements, our work presents an ideal platform for the investigation of these unresolved theoretical issues. Finally, our demonstration of emergent phenomena through wave-based interactions illustrates a path for developing non-equilibrium materials with lifelike properties that would be difficult to achieve through static means. Such an approach could ultimately lead to the development of artificial self-replicating and evolving systems[47,48] for the creation of synthetic living materials[49] as well as collective matter displaying non-algorithmic intelligence for human-like decision making[50].

Methods

Methods, including statements of data availability and any associated accession codes and references, are available in the online version of this paper.

Received 11 January 2017; accepted 17 May 2017; published online 19 June 2017

References

1. Bhat, H. L. *Introduction to Crystal Growth: Principles and Practice* (CRC Press, 2014).
2. Kalsin, A. M. *et al*. Electrostatic self-assembly of binary nanoparticle crystals with a diamond-like lattice. *Science* **312,** 420–424 (2006).
3. Dong, A., Chen, J., Vora, P. M., Kikkawa, J. M. & Murray, C. B. Binary nanocrystal superlattice membranes self-assembled at the liquid–air interface. *Nature* **466,** 474–477 (2010).
4. van Blaaderen, A., Ruel, R. & Wiltzius, P. Template-directed colloidal crystallization. *Nature* **385,** 321–324 (1997).
5. Leunissen, M. E. *et al*. Ionic colloidal crystals of oppositely charged particles. *Nature* **437,** 235–240 (2005).
6. de Nijs, B. *et al*. Entropy-driven formation of large icosahedral colloidal clusters by spherical confinement. *Nat. Mater.* **14,** 56–60 (2014).
7. Grzybowski, B. A., Wilmer, C. E., Kim, J., Browne, K. P. & Bishop, K. J. M. Self-assembly: from crystals to cells. *Soft Matter* **5,** 1110–1128 (2009).
8. Karsenti, E. Self-organization in cell biology: a brief history. *Nat. Rev. Mol. Cell Biol.* **9,** 255–262 (2008).
9. Shimoyama, N., Sugawara, K., Mizuguchi, T., Hayakawa, Y. & Sano, M. Collective motion in a system of motile elements. *Phys. Rev. Lett.* **76,** 3870–3873 (1996).
10. Couzin, I. D. & Franks, N. R. Self-organized lane formation and optimized traffic flow in army ants. *Proc. R. Soc. B* **270,** 139–146 (2003).
11. Mateus, A. M., Gorfinkiel, N. & Arias, A. M. Origin and function of fluctuations in cell behaviour and the emergence of patterns. *Semin. Cell Dev. Biol.* **20,** 877–884 (2009).
12. Mora, T. *et al*. Local equilibrium in bird flocks. *Nat. Phys.* **12,** 1153–1157 (2016).
13. Whitesides, G. M. & Grzybowski, B. Self-assembly at all scales. *Science* **295,** 2418–2421 (2002).
14. Kondepudi, D. & Prigogine, I. *Modern Thermodynamics: From Heat Engines to Dissipative Structures* (John Wiley, 2014).
15. Fialkowski, M. *et al*. Principles and implementations of dissipative (dynamic) self-assembly. *J. Phys. Chem. B* **110,** 2482–2496 (2006).
16. Osterman, N. *et al*. Field-induced self-assembly of suspended colloidal membranes. *Phys. Rev. Lett.* **103,** 228301 (2009).
17. Grzybowski, B. A., Stone, H. A. & Whitesides, G. M. Dynamic self-assembly of magnetized, millimetre-sized objects rotating at a liquid–air interface. *Nature* **405,** 1033–1036 (2000).
18. Snezhko, A., Aranson, I. S. & Kwok, W.-K. Surface wave assisted self-assembly of multidomain magnetic structures. *Phys. Rev. Lett.* **96,** 078701 (2006).
19. Snezhko, A. & Aranson, I. S. Magnetic manipulation of self-assembled colloidal asters. *Nat. Mater.* **10,** 698–703 (2011).
20. Lehn, J.-M. Toward self-organization and complex matter. *Science* **295,** 2400–2403 (2002).
21. England, J. L. Dissipative adaptation in driven self-assembly. *Nat. Nanotech.* **10,** 919–923 (2015).
22. Perunov, N., Marsland, R. A. & England, J. L. Statistical physics of adaptation. *Phys. Rev. X* **6,** 021036 (2016).
23. Snezhko, A., Belkin, M., Aranson, I. S. & Kwok, W.-K. Self-assembled magnetic surface swimmers. *Phys. Rev. Lett.* **102,** 118103 (2009).
24. Boekhoven, J. *et al*. Dissipative self-assembly of a molecular gelator by using a chemical fuel. *Angew. Chem.* **122,** 4935–4938 (2010).
25. Bricard, A., Caussin, J.-B., Desreumaux, N., Dauchot, O. & Bartolo, D. Emergence of macroscopic directed motion in populations of motile colloids. *Nature* **503,** 95–98 (2013).
26. Palacci, J., Sacanna, S., Steinberg, A. P., Pine, D. J. & Chaikin, P. M. Living crystals of light-activated colloidal surfers. *Science* **339,** 936–940 (2013).
27. Martinez-Pedrero, F., Ortiz-Ambriz, A., Pagonabarraga, I. & Tierno, P. Colloidal microworms propelling via a cooperative hydrodynamic conveyor belt. *Phys. Rev. Lett.* **115,** 138301 (2015).
28. Solis, K. J. & Martin, J. E. Complex magnetic fields breathe life into fluids. *Soft Matter* **10,** 9136–9142 (2014).
29. Maiti, S., Fortunati, I., Ferrante, C., Scrimin, P. & Prins, L. J. Dissipative self-assembly of vesicular nanoreactors. *Nat. Chem.* **8,** 725–731 (2016).
30. Vlasov, Y. A., Bo, X.-Z., Sturm, J. C. & Norris, D. J. On-chip natural assembly of silicon photonic bandgap crystals. *Nature* **414,** 289–293 (2001).
31. Hynninen, A.-P., Thijssen, J. H. J., Vermolen, E. C. M., Dijkstra, M. & van Blaaderen, A. Self-assembly route for photonic crystals with a bandgap in the visible region. *Nat. Mater.* **6,** 202–205 (2007).
32. Lemoult, F., Kaina, N., Fink, M. & Lerosey, G. Wave propagation control at the deep subwavelength scale in metamaterials. *Nat. Phys.* **9,** 55–60 (2012).
33. Alonso-Redondo, E. *et al*. A new class of tunable hypersonic phononic crystals based on polymer-tethered colloids. *Nat. Commun.* **6,** 8309 (2015).
34. Beatus, T., Tlusty, T. & Bar-Ziv, R. Phonons in a one-dimensional microfluidic crystal. *Nat. Phys.* **2,** 743–748 (2006).
35. Timonen, J. V. I., Latikka, M., Leibler, L., Ras, R. H. A. & Ikkala, O. Switchable static and dynamic self-assembly of magnetic droplets on superhydrophobic surfaces. *Science* **341,** 253–257 (2013).
36. Tretiakov, K. V., Bishop, K. J. M. & Grzybowski, B. A. The dependence between forces and dissipation rates mediating dynamic self-assembly. *Soft Matter* **5,** 1279–1284 (2009).

37. Joannopoulos, J. D., Johnson, S. G., Winn, J. N. & Meade, R. D. *Photonic Crystals: Molding the Flow of Light* 2nd edn (Princeton Univ. Press, 2011).
38. Dholakia, K. & Zemánek, P. Gripped by light: optical binding. *Rev. Mod. Phys.* **82,** 1767–1791 (2010).
39. Karásek, V. *et al*. Long-range one-dimensional longitudinal optical binding. *Phys. Rev. Lett.* **101,** 143601 (2008).
40. Frawley, M. C., Gusachenko, I., Truong, V. G., Sergides, M. & Chormaic, S. N. Selective particle trapping and optical binding in the evanescent field of an optical nanofiber. *Opt. Express* **22,** 16322–16334 (2014).
41. Strogatz, S. H. *Nonlinear Dynamics And Chaos: With Applications To Physics, Biology, Chemistry, And Engineering* (Westview Press, 2001).
42. von Freymann, G., Kitaev, V., Lotsch, B. V. & Ozin, G. A. Bottom-up assembly of photonic crystals. *Chem. Soc. Rev.* **42,** 2528–2554 (2013).
43. Prather, D. W. *Photonic Crystals, Theory, Applications and Fabrication* (John Wiley, 2009).
44. Martyushev, L. M. & Seleznev, V. D. Maximum entropy production principle in physics, chemistry and biology. *Phys. Rep.* **426,** 1–45 (2006).
45. Ross, J., Corlan, A. D. & Müller, S. C. Proposed principles of maximum local entropy production. *J. Phys. Chem. B* **116,** 7858–7865 (2012).
46. Martyushev, L. M. & Seleznev, V. D. The restrictions of the maximum entropy production principle. *Phys. Stat. Mech. Appl.* **410,** 17–21 (2014).
47. Deplazes, A. & Huppenbauer, M. Synthetic organisms and living machines. *Syst. Synth. Biol.* **3,** 55–63 (2009).
48. Deplazes, A. Piecing together a puzzle. *EMBO Rep.* **10,** 428–432 (2009).
49. Szostak, J. W., Bartel, D. P. & Luisi, P. L. Synthesizing life. *Nature* **409,** 387–390 (2001).
50. Haken, H. *Principles of Brain Functioning: A Synergetic Approach to Brain Activity, Behavior and Cognition* (Springer Science & Business Media, 2013).

Acknowledgements

The experimental part of this work is supported by the Office of Naval Research (ONR) MURI program under Grant No. N00014-13-1-0631; the numerical calculation and energy analysis is supported by the 'Light-Material Interactions in Energy Conversion' Energy Frontier Research Center funded by the US Department of Energy, Office of Science, Office of Basic Energy Sciences under Award Number DE-AC02-05CH11231.

Author contributions

N.B. and C.R. designed and conducted experiments and performed the theoretical investigation; M.D. performed COMSOL simulations; R.Z. provided theoretical guidance; X.Z. and Y.W. guided the research. All authors contributed to writing the manuscript.

Additional information

Supplementary information is available in the online version of the paper. Reprints and permissions information is available online at www.nature.com/reprints. Publisher's note: Springer Nature remains neutral with regard to jurisdictional claims in published maps and institutional affiliations. Correspondence and requests for materials should be addressed to X.Z.

Competing financial interests

The authors declare no competing financial interests.

Methods

Acoustic set-up. The acoustic waveguide consists of a 2-m-long, 2.2-cm-diameter transparent acrylic tube with funnel-shaped input and output (Supplementary Fig. 7). Twenty-cm-long ramps made out of PDMS are constructed inside the waveguide to hold a 5-mm-deep pool of viscous liquid (50% glycerin–water solution with 0.125 wt% Tween-20 surfactant). The ramps are designed to adiabatically shrink the waveguide mode and to hold the liquid pool. The acoustic source consists of off-the-shelf computer speakers, with maximum output power of 93 dB, that are controlled through Matlab code. In all the experiments we use a 3.9 kHz frequency to drive self-assembly, except in the reconfigurability data sets shown in Figs 1d and 2d where we switch between 3.9 kHz and 4.3 kHz, which are two frequencies located near peaks of the speaker's emission spectrum (Supplementary Fig. 8). Transmission spectra are acquired by periodically sending a frequency-chirped probe, which we register using a microphone at the end of the waveguide. Before each experiment, we obtain an empty waveguide spectrum and use it to normalize the transmission spectrum obtained during self-assembly. To improve the system performance, the output funnel of our waveguide is fitted with cotton to absorb the transmitted acoustic waves and prevent any unwanted reflections that would create stationary-wave patterns. Supplementary Fig. 9 shows the smooth trajectory of a single particle that is pushed along the whole length of the waveguide, illustrating that there is no stationary-wave pattern. This trajectory also demonstrates that transmission loss is minimal for our waveguide. A small amount of absorbing cotton is also introduced at the speaker input to avoid Fabry–Perot resonances due to interference between the ensemble and the speaker facet (Supplementary Fig. 10) that may appear in the transmission spectra.

Meniscus particles. Scattering particles are made from plastic straws that are cut to 10 mm in height and elongated into 8×12 mm elliptic cylinders, $D_S = 12$ mm. These cylinders are glued to a 9×15 mm piece of rigid plastic and sealed with glue to a fitted piece of plastic on top. We glue a 5 mm steel rod on top of the particles, enabling magnetic loading and placement along the waveguide. A photograph of a particle is shown in Supplementary Fig. 11. These particles behave as sub-wavelength scatterers with respect to the drive (wavelength of 88 mm), which prevents the occurrence of resonant effects. We estimate the particle absorption to be 1% by fitting the transmission spectrum of a 12-particle self-assembled system to a numeric model that includes absorption (Supplementary Fig. 12). COMSOL modelling indicates that the particle reflection coefficient is approximately 4%. In experiments, we characterize all of the particles speeds in an empty waveguide and choose a set of particles with similar speeds to perform the self-assembly. For the data sets in Figs 1 and 2, the 12 particles have speeds of [9.5, 9.8, 10.2, 10.3, 9.8, 9.6, 9.4, 10.8, 9.2, 10.0, 9.8, 10.1] cm min^{-1}. For the data sets in Fig. 4, the three particles chosen have speeds of [8.7, 8.6, 8.8] cm min^{-1}. Particles are loaded into the waveguide in the order listed and we monitor their positions using a webcam combined with a subpixel detection technique. We are required to compensate for particle inhomogeneity in Fig. 4a to match the locations of the attractors. We offset $D_2(t)$ and $D_3(t)$ by 5% and 2% of λ_0, respectively.

Theory. The system is composed of N scattering particles sharing the same reflection coefficient in intensity, R, and distributed along the waveguide (Fig. 1a). The mass of the particles are assumed very small, and thus inertial effects are neglected. While the kinetic energy of the particles is smaller than the absorbed wave energy, this absorption produces a negligible increase in temperature. The kinetics of our system is driven entirely by the transfer of wave momentum due to scattering. For a single particle, the wave pressure force is proportional to $2R + A$, where $A/2R = 1/8 \ll 1$. Thus, the contribution of absorption to wave scattering is negligible and we assume the particle to be lossless. Therefore, each particle satisfies:

$$m\frac{\mathrm{d}^2 x_n}{\mathrm{d}t^2} = -\gamma v_n + F_n \approx 0 \tag{4}$$

where m, x_n, γ, v_n and F_n are the mass, position, viscous damping, velocity, and pressure force associated with the nth particle, respectively. The acoustic field is spatially confined to a single mode, which allows us to describe the scattering through a transfer matrix (TM) approach. Between particles $n-1$ and n we note A_n, I_n, and Φ_n as the field, intensity, and accumulated phase, respectively (see Supplementary Information). Using the TM formalism, the complex field and the intensity are respectively decomposed into a forward and a backward component, $[A_n^+, A_n^-]^T$ and $[I_n^+, I_n^-]^T$. At steady state the intensities at both extremities read $I_1 = [1, R_S]$ and $I_{N+1} = [T_S, 0]$ (see Fig. 1a), where R_S is the reflection coefficient in intensity of the whole structure and T_S the corresponding coefficient in transmission. The pressure force exerted on the particles is responsible for a drop in average intensity across each particle, which is derived as $F_n = \langle I_n \rangle - \langle I_{n+1} \rangle = |A_n^+|^2 + |A_n^-|^2 - (|A_{n+1}^+|^2 + |A_{n+1}^-|^2)$.

Numerical modelling. The scattering properties of our particle–waveguide system are simulated in 3D with COMSOL software to extract the intensity reflection coefficient $R = 4\%$ with our geometry. The temporal evolution of our system is numerically investigated using a TM approach that includes the effects of particle absorption (Supplementary Fig. 6). For a given organization of the particles, we obtain the field using the TM model. The resulting forces on individual particles are then derived and the new positions are obtained from Newton's equation, neglecting inertial effects.

Data availability. The data that support the findings of this paper are available from the corresponding author on request.